

The effect of lithology on the relationship between denudation rate and chemical weathering pathways. Evidence from the eastern Tibetan Plateau.

Aaron Bufo¹, Kristen L. Cook¹, Albert Galy², Hella Wittmann¹, Niels Hovius^{1,3}

¹German Research Center for Geosciences, Potsdam 14473, Germany

²Centre de Recherches Pétrographiques et Géo-chimiques, CNRS, Université de Lorraine, 54500 Nancy, France.

³Institute of Geosciences, Potsdam University, Potsdam 14476, Germany

Correspondence to: Aaron Bufo (aaronbufo@gmail.com)

10 **Abstract.** The denudation of rocks in mountain belts exposes a range of fresh minerals to the surface of the Earth that are chemically weathered by acidic and oxygenated fluids. The impact of the resulting coupling between denudation and weathering rates fundamentally depends on the types of minerals that are weathering. Whereas silicate weathering sequesters CO₂, the combination of sulfide oxidation and carbonate dissolution emits CO₂ to the atmosphere. Here, we combine the concentrations of dissolved major elements in stream waters with ¹⁰Be basin-wide denudation rates from 35 small catchments in eastern Tibet to elucidate the importance of lithology in modulating the relationships between denudation rate, chemical weathering pathways, and CO₂ consumption or release. Our catchments span three orders of magnitude in denudation rate in low-grade flysch, high grade metapelites, and granitoid rocks. For each stream, we estimate the concentrations of solutes sourced from silicate weathering, carbonate dissolution, and sulfide oxidation using a mixing model. We find that for all lithologies, cation concentrations from silicate weathering are largely independent of denudation rate, but solute concentrations from carbonates and, where present, sulfides increase with increasing denudation rate. With increasing denudation rates, weathering may, therefore, shift from consuming to releasing CO₂ in both (meta)sedimentary and granitoid lithologies. For a given denudation rate, we find that we report 5 – 10-times catchments draining high-grade metamorphic rocks have systematically higher dissolved solid concentrations and inferred weathering fluxes in catchments underlain by (meta)sedimentary rock compared to of sulfate from sulfide weathering than catchments containing weakly metamorphosed sediments granitoid lithologies, even though climatic and topographic parameters do not vary systematically between these catchments. Moreover, our data provide tentative evidence that sulfate concentrations in these catchments are potentially more sensitive to denudation rate. We propose that changes in the sulfur oxidation state during prograde metamorphism of pelites in the mid-crust could lead to sulfate reduction that is even more complete than in low-grade sediments and provides a larger sulfide source for oxidation upon re-exposure of the rocks. In this case Thus, the elevated concentration of sulfate in catchments draining high-grade metapelites would suggest that varying proportions of exposed exposure of an increasing fraction of

Formatted: English (United Kingdom)

~~metamorphic (meta)sedimentary and igneous~~ rocks during orogenesis could lead to ~~substantial a boost in~~ changes in the ~~sequestration and release of~~ ~~release of~~ CO₂ that ~~is~~ ~~are~~ independent of denudation rate.

1 Introduction

35 The relationship between chemical weathering and CO₂ drawdown modulates the global carbon cycle and Earth's climate (Berner et al., 1983; Walker et al., 1981). Uplift and denudation of rock control the supply of unweathered minerals to the surface of the Earth and impact the residence time of these minerals in the weathering zone (e.g. Gabet and Mudd, 2009; Hilley et al., 2010; Riebe et al., 2001; West et al., 2005). Thus, increases in denudation rates can boost chemical weathering and ultimately affect Earth's climate (Caves Rügenstein et al., 2019; Hilton and West, 2020; Kump and Arthur, 1997; Raymo and
40 Ruddiman, 1992). The impact of chemical weathering on the attendant emission or drawdown of CO₂ depends on the relative importance of different weathering pathways (Berner et al., 1983; Bufe et al., 2021; Calmels et al., 2007; Hartmann et al., 2009; Hilton and West, 2020; Torres et al., 2016; Torres et al., 2014). Weathering of silicate minerals by carbonic acid consumes CO₂ from the atmosphere and drives the sequestration of this carbon ~~into marine carbonates over timescales longer~~
45 ~~than marine carbonate compensation~~ (Walker et al., 1981). In turn, sulfuric acid produced by the oxidation of pyrite can drive rapid dissolution of carbonate minerals that releases CO₂ into the atmosphere ~~over timescales that exceed the timescale of~~
~~carbonate compensation in the Ocean~~ (Calmels et al., 2007; Das et al., 2012; Spence and Telmer, 2005; Torres et al., 2014), ~~although the impact of that inorganic carbon source and its link to the organic carbon cycle remain debated~~ (Maffre et al.,
50 2021; Torres et al., 2014). Weathering of silicate minerals by sulfuric acid and of carbonate minerals by carbonic acid are carbon neutral (Calmels et al., 2007; Spence and Telmer, 2005). Importantly, carbonates and sulfides weather several orders
of magnitude faster than silicate minerals (Berner, 1978; Morse and Arvidson, 2002; Williamson and Rimstidt, 1994), such
that sulfuric acid-driven carbonate weathering dominates the total solute flux even in lithologies with small fractions of pyrite
or carbonate (Anderson et al., 2000; Bufe et al., 2021; Calmels et al., 2007; Das et al., 2012; Emberson et al., 2016b; Jacobson
and Blum, 2003; Kemeny et al., 2021; Relp et al., 2021; Spence and Telmer, 2005; Torres et al., 2016).

The dependence of chemical weathering on mineralogy implies a lithologic control on the balance of CO₂ drawdown and CO₂
55 release by weathering reactions. Fresh and fine-grained mafic rocks, such as basalts, exhibit some of the fastest silicate
weathering rates on the planet and contribute disproportionately to global silicate weathering fluxes (Dessert et al., 2003;
Gaillardet et al., 1999; Ibarra et al., 2016; Li et al., 2016). Felsic igneous rocks typically weather more slowly, but silicate
weathering in these rocks is also thought to be sensitive to denudation rates (Riebe et al., 2004; West et al., 2005). In contrast,
60 weathering of siliciclastic (meta)sedimentary rocks is often dominated by the dissolution of minor carbonate and sulfides
(Anderson et al., 2000; Blattmann et al., 2019; Bufe et al., 2021; Calmels et al., 2007; Das et al., 2012; Emberson et al., 2016b;
Jacobson and Blum, 2003; Kemeny et al., 2021; Relp et al., 2021; Spence and Telmer, 2005; Torres et al., 2016), and rapid

denudation and exposure of these rocks can drive CO₂ release from weathering (Bufe et al., 2021; Calmels et al., 2007; Märki et al., 2021; Spence and Telmer, 2005; Torres et al., 2016; Torres et al., 2014). Carbonate dissolution also dominates weathering of carbonate-rich sediments (Erlanger et al., 2021; Gaillardet et al., 2018; Gaillardet et al., 1999), but the role of sulfide oxidation and, therefore, the impact of carbonate weathering on the long-term CO₂-cycle can be limited in these rocks (Erlanger et al., 2021; Gaillardet et al., 2018; Gaillardet et al., 1999).

Even though lithology exerts a fundamental control on the link between weathering and Earth's carbon cycle, few studies have directly compared and quantified the impact of lithologic variation on the link between physical denudation and chemical weathering and on the importance of different weathering pathways. Such knowledge is important in the context of mountain building, as ongoing exhumation progressively exposes successions of different lithologies to chemical weathering (Hilton and West, 2020). Landscape-scale weathering fluxes are typically estimated by measuring the solute concentration and runoff in rivers that integrate water fluxes across the upstream catchment (Drever and Clow, 2018; Drever and Zobrist, 1992; Gaillardet et al., 1999; White and Blum, 1995). In many settings, denudation gradients coincide with gradients in precipitation, temperature, tectonics, biomass, and/or substrate properties such as fracture density or metamorphic grade (Dixon et al., 2016); gradients that affect weathering kinetics independently of denudation rates (Drever and Zobrist, 1992; Gaillardet et al., 2018; Godsey et al., 2019; Guo et al., 2019; Ibarra et al., 2016; Li et al., 2016; Oeser and von Blanckenburg, 2020; Uhlig and von Blanckenburg, 2019; White and Blum, 1995). These co-variations can complicate the interpretation of changes in weathering. Here, we investigate the impact of lithologic variations on chemical weathering across a nearly three-order of magnitude wide denudation rate gradient along the eastern margin of the Tibetan Plateau that includes three well-separated groups of lithology (Fig. 1) and relatively small changes in precipitation, elevation, and temperature (Fig. 2, Table S1).

2 Geologic setting

On the eastern Tibetan Plateau west of the Sichuan Basin lies the Songpan-Ganze (or Songpan-Garzê) fold belt, which formed during the late Triassic to early Jurassic closure of part of the Paleotethys ocean (Burchfiel et al., 1995; Chen et al., 2007; Weller et al., 2013). The Songpan-Ganze terrane is characterized by a 5 – 15 km thick sequence of tightly folded Triassic flysch that overlies Paleozoic metasedimentary rocks and Precambrian basement (Roger et al., 2010; Weller et al., 2013) (Fig. 1). These units have been intruded by granitoids during both the Mesozoic and Cenozoic. Reactivation of the region during the Cenozoic Indo-Eurasian collision formed zones of rapid uplift and denudation within and at the eastern edge of the slowly eroding Tibetan plateau. Here, we focus on the southeastern part of the Songpan-Ganze fold belt in the region around the Danba Structural culmination and the zone of rapid uplift ~~entered~~centred around Gongga Shan (Fig. 1). In this area, in-situ ¹⁰Be-derived basin-wide denudation rates vary more than 200-fold over a distance of 100-200 km, from 0.018 mm/yr on the plateau margin (Fig. 1) to 7 mm/yr around Mt Gongga and the Danba structural culmination over a distance of 100-200 km (Cook et al., 2018; Ouimet et al., 2009) (Fig. 1). This variation of denudation rates is reflected in by the topography with variations of basin averaged relief between 340 m – 5260 m and basin-averaged slopes of 10° – 37.9° low relief and gentle

[slopes on the plateau margin \(Fig. 1\) and steep slopes and high relief around Mt Gongga and the Danba structural culmination.](#)

95 The region features three principal lithologic groups. Most of the area exposes the Triassic Songpan-Ganze flysch, a sequence of deep sea turbidites that is unmetamorphosed or weakly metamorphosed over large areas but can reach greenschist facies close to Gongga Shan and the Danba Structural culmination (Burchfiel et al., 1995; Chen et al., 2007). The underlying Paleozoic sequence is exposed in the Danba structural culmination and in the Longmen Shan and consists of a passive margin sequence, which has undergone metamorphism up to amphibolite facies (Huang et al., 2003; Weller et al., 2013). Finally, 100 granitic rocks of a range of ages from Precambrian to Cenozoic are exposed throughout the area (Roger et al., 2010; Roger et al., 2004; Searle et al., 2016) (Fig. 1, Table S1). Rocks within each one of these three broad lithologic groups have varying compositions, but the difference in chemical compositions and mineralogy between these three lithologic groups is greater than the variability within each one of the groups (Chen et al., 2007; Jiang et al., 2018; Weller et al., 2013) (Table S3, Fig. 3). Moreover, minor carbonate and sulfide phases occur in varying proportions in these dominantly silicate lithologies (Chen et al., 2007; Jiang et al., 2018; Weller et al., 2013). 105

The region is characterized by a cold and humid climate with a pronounced wet monsoon season during the summer months and drier winter months. Mean annual precipitation rates derived by the Tropical Rainfall Measuring Mission (TRMM) vary ~4-5-fold between 300 – 1340 mm/yr (Bookhagen and Burbank, 2010) (Fig. [2B2b](#)). This range of precipitation values is very 110 similar to the range of runoff values previously estimated for small catchments around the Gongga Shan (Table 1 in Jiang et al. (2018)). Our sampled catchments [feed the Dadu, Min, and the Yalongjiang rivers, tributaries to the Yangtze river. They are all headwater catchments with](#) ~~that fall within~~ [within](#) a relatively narrow elevation window with catchment averaged elevations of 3500-4800 m with three exceptions at lower mean elevations of 2600 – 2800 m (Fig. [2A2a](#), Table S1). ~~The treeline lies between ~3500 – 4100m. Thus, the majority of catchments spans across the treeline and includes forested areas, grasslands and rocky slopes~~ [majority of the sampled catchment area lies above the treeline and is sparsely vegetated.](#) Neither 115 the elevation, nor the annual precipitation in the studied catchments or the temperature of sampled stream waters correlate strongly with the denudation rate across the area (Fig. 2)

3 Methods

3.1 Sample collection and analysis

120 We collected water samples from 35 small catchments around the region of Mt Gongga and the Danba structural culmination (Fig. 1, Table S1). Water samples were collected in mid-May 2018, prior to the rainy season, over a period of 5 days when all catchments were subject to similar hydrological conditions. Most of the sampled catchments drain a single lithologic group: Thirteen catchments drain the Triassic flysch that is dominantly composed of unmetamorphosed or weakly metamorphosed mixed carbonate-siliciclastic sediments. Only two of the flysch catchments include rocks that have been metamorphosed to

125 garnet-bearing greenschists (S18-35 & S18-36, Fig. 3C3c). Eleven catchments drain granitic rocks, and six catchments drain
high-grade Paleozoic and Precambrian metasedimentary rocks, whereas five catchments drain a mix of granitic rocks and
Triassic flysch (Fig. 3C3c, Table S1). Samples were taken as close to sites sampled for cosmogenic nuclide-derived denudation
rates (Cook et al., 2018) as possible, and upstream of potential major anthropogenic influences. Water samples were filtered
in situ with single-use 0.2 μm filters and collected in HDPE bottles. Aliquots for cation analysis were acidified on-site to a pH
of ~2 with 3M ultrapure HNO_3 . Temperature, pH, and conductivity were measured in the field using a WTW Multi 3430
multimeter.

Anion and cation analyses were conducted at the GFZ Potsdam on a Dionex ICS-1100 Ion Chromatograph and a Varian 720
ICP-OES, respectively, following the procedure described in Bufe et al. (2021). The concentration of bicarbonate was
estimated by charge balance. Such estimation is reasonable in active mountain settings where organic acids are scarce and
estimates of bicarbonate from charge balance are within uncertainty of alkalinity values from titrations (Galy and France-
Lanord, 1999). Analytical uncertainties for cation analyses were derived from the largest deviation of the calibration standards
from the calibration line. For anions, uncertainty estimates were derived from the standard deviation of three repeat
measurements (Table S2).

3.2 Unmixing of solute sources

140 We consider four major sources of cations to rivers in the study area: Silicate weathering, carbonate weathering, cyclic
~~contributions-~~ (assumed to be dominated by wet precipitation), and hot springs contributions (Table 1). ~~Major-~~We assume that
~~evaporites are a minor component of the dissolved solids: (i) Existing petrologic and geochemical studies do not report~~
~~evaporites deposits in -are not reported in-~~ the upper Triassic flysch or in the Paleozoic metamorphic rocks around the Danba
Structural culmination (Chen et al., 2007; Jiang et al., 2018), (ii) ~~except for one sample, chloride concentrations range between~~
145 ~~4-20 $\mu\text{mol/L}$ and are thus well within the range of concentrations expected for atmospheric chloride input (Gaillardet et al.,~~
~~1999).~~ (Jiang et al., 2018) and (iii) ~~the ratios of $\left[\frac{\text{Ca}^{2+}}{\text{Na}^+}\right]$ concentrations are higher than expected for typical evaporite deposits~~
(Chen et al., 2007; Gaillardet et al., 1999; Jiang et al., 2018). ~~Any minor salt input that is not captured by the-~~ Moreover, we
assume that secondary precipitation of carbonate minerals is negligible in the area. This assumption is based on the observation
that all samples are either undersaturated with respect to calcium carbonate or are within uncertainty of saturation, except for
150 two Flysch basins that suggest slightly super-saturated conditions (Fig. A1).

We used a 4-endmember inverse model to unmix these contributions based on the relative concentration of the three major
soluble cations (Na^+ , Ca^{2+} , and Mg^{2+}) and chloride (Cl^-) (Bufe et al., 2021; Gaillardet et al., 1999; Kemeny and Torres,
2021; Moon et al., 2014; Torres et al., 2016). The mixing model requires that each one of the endmembers is unique and,
therefore, occupies a range of compositions that is distinct from the composition of other endmembers in the considered space
155 (Fig. 3a-bA-B). In the model, we minimized the following set of equations using the constrained linear least squares solver
lsqin in MATLAB:

$$\left[\frac{X}{Ca^{2+}}\right]_{spl} = \alpha_{Ca,sil} \left[\frac{X}{Ca^{2+}}\right]_{sil} + \alpha_{Ca,carb} \left[\frac{X}{Ca^{2+}}\right]_{carb} + \alpha_{Ca,cy} \left[\frac{X}{Ca^{2+}}\right]_{cy} + \alpha_{Ca,hs} \left[\frac{X}{Ca^{2+}}\right]_{hs}, \quad (1-3)$$

With $X = Na^+$, $X = Mg^{2+}$, and $X = Mg^{2+}Cl^-$ (three equations) under the conditions that:

$$\alpha_{Ca,sil} + \alpha_{Ca,carb} + \alpha_{Ca,cy} + \alpha_{Ca,hs} = 1 \quad (4)$$

160 and

$$0 \leq \alpha_{Ca,sil} \leq 1; 0 \leq \alpha_{Ca,carb} \leq 1; 0 \leq \alpha_{Ca,cy} \leq 1; 0 \leq \alpha_{Ca,hs} \leq 1 \quad (5)$$

Here, $\left[\frac{X}{Ca^{2+}}\right]$ is the ratio of concentrations of ion X and calcium, and $\alpha_{Ca,Y}$ is the fraction of calcium sourced from endmember Y . The subscript spl denotes the sampled ratio in the river water. The endmember subscripts sil , $carb$, cy , and hs denote contributions from silicate, carbonate, cyclic (precipitation), and hotspring sources respectively. and subscript mix denotes the sampled mixed ratio in the river water.

165

Equations 1-5 were then solved separately for each of the 35 samples based on the input endmember compositions ($\left[\frac{X}{Ca^{2+}}\right]_{sil,carb,cy,hs}$, see Table 1) and the measured ratios ($\left[\frac{X}{Ca^{2+}}\right]_{spl}$, see Table S2). Note that one out of three different silicate endmembers was chosen for each sample, depending on the lithology in the sampled catchments (Table 1, Table S1). Where catchments contain a mix of different lithologies (for example S18-22 and S18-23, see Table S2), the input silicate endmember was determined by the average between the silicate endmembers from the lithologies weighted by the areal coverage of each lithology class in the catchment (see Table S1).

170

In order to represent the uncertainty of the endmember compositions in the inversion result, we implemented a Monte Carlo approach and ran 100,000 iterations of the inversion for each sample. For each iteration, we input an a-priori estimate of the endmember ratios and their uncertainty (Table 1). We then randomly picked a set of four endmembers from a normal distribution with mean and standard deviation defined by the a-priori endmember estimate and its uncertainty (Table 1). For the hotspring endmember, we instead picked from a uniform distribution defined by a minimum and maximum estimate (see below, Table 1). For each sample (35 samples) and each iteration (100,000 iterations), we used a reduced chi-squared statistic to estimate the goodness of fit of that sample and iteration. The goodness of fit, χ_{total}^2 , was based on the sum of (1) χ_{spl}^2 , the squared distances between the modelled and elemental ratios predicted by that particular iteration $\left[\frac{X}{Ca^{2+}}\right]_{spl}^{model}$ and the sampled elemental ratios sampled $\left[\frac{X}{Ca^{2+}}\right]_{spl}$ ratios normalized by the variance uncertainty in the samples in the sampled ratio $\sigma_{\left[\frac{X}{Ca^{2+}}\right]_{spl}}$ (see Table S2 for data and uncertainties) and (2)

175

$\chi_{endmember}^2$, the squared distances between the randomly picked endmember ratios picked from the normal distribution $\left[\frac{X}{Ca^{2+}}\right]_{sil,carb,cy,hs}^{model}$ ratios and the mean average $\left[\frac{X}{Ca^{2+}}\right]_{sil,carb,cy,hs}$ endmember value normalized by the input value normalized

180

Formatted: Tab stops: 7 cm, Left

by the variance-uncertainty of the input endmember values $\sigma_{\left[\frac{X}{Ca^{2+}}\right]_{sil,carb,cy,hs}}$ (see Table 1 for endmember values and

185 uncertainties) with:

$$\chi_{splt}^2 = \left(\frac{\left[\frac{Na^+}{Ca^{2+}}\right]_{splt}^{model} - \left[\frac{Na^+}{Ca^{2+}}\right]_{splt}}{\sigma_{\left[\frac{Na^+}{Ca^{2+}}\right]_{splt}}} \right)^2 + \left(\frac{\left[\frac{Mg^{2+}}{Ca^{2+}}\right]_{splt}^{model} - \left[\frac{Mg^{2+}}{Ca^{2+}}\right]_{splt}}{\sigma_{\left[\frac{Mg^{2+}}{Ca^{2+}}\right]_{splt}}} \right)^2 + \left(\frac{\left[\frac{Cl^-}{Ca^{2+}}\right]_{splt}^{model} - \left[\frac{Cl^-}{Ca^{2+}}\right]_{splt}}{\sigma_{\left[\frac{Cl^-}{Ca^{2+}}\right]_{splt}}} \right)^2 \quad (6)$$

and

$$\chi_{endmember}^2 = \left(\frac{\left[\frac{Na^+}{Ca^{2+}}\right]_{sil}^{model} - \left[\frac{Na^+}{Ca^{2+}}\right]_{sil}}{\sigma_{\left[\frac{Na^+}{Ca^{2+}}\right]_{sil}}} \right)^2 + \left(\frac{\left[\frac{Mg^{2+}}{Ca^{2+}}\right]_{sil}^{model} - \left[\frac{Mg^{2+}}{Ca^{2+}}\right]_{sil}}{\sigma_{\left[\frac{Mg^{2+}}{Ca^{2+}}\right]_{sil}}} \right)^2 + \left(\frac{\left[\frac{Mg^{2+}}{Ca^{2+}}\right]_{carb}^{model} - \left[\frac{Mg^{2+}}{Ca^{2+}}\right]_{carb}}{\sigma_{\left[\frac{Mg^{2+}}{Ca^{2+}}\right]_{carb}}} \right)^2 +$$

$$\left(\frac{\left[\frac{Na^+}{Ca^{2+}}\right]_{cy}^{model} - \left[\frac{Na^+}{Ca^{2+}}\right]_{cy}}{\sigma_{\left[\frac{Na^+}{Ca^{2+}}\right]_{cy}}} \right)^2 + \left(\frac{\left[\frac{Mg^{2+}}{Ca^{2+}}\right]_{cy}^{model} - \left[\frac{Mg^{2+}}{Ca^{2+}}\right]_{cy}}{\sigma_{\left[\frac{Mg^{2+}}{Ca^{2+}}\right]_{cy}}} \right)^2 + \left(\frac{\left[\frac{Cl^-}{Ca^{2+}}\right]_{cy}^{model} - \left[\frac{Cl^-}{Ca^{2+}}\right]_{cy}}{\sigma_{\left[\frac{Cl^-}{Ca^{2+}}\right]_{cy}}} \right)^2 \quad (7)$$

190 where

$$\left[\frac{X}{Ca^{2+}}\right]_{splt}^{model} = \alpha_{Ca,sil}^{model} \left[\frac{X}{Ca^{2+}}\right]_{sil}^{model} + \alpha_{Ca,carb}^{model} \left[\frac{X}{Ca^{2+}}\right]_{carb}^{model} + \alpha_{Ca,cy}^{model} \left[\frac{X}{Ca^{2+}}\right]_{cy}^{model} + \alpha_{Ca,hs}^{model} \left[\frac{X}{Ca^{2+}}\right]_{hs}^{model} \quad (8)$$

The superscript *model* refers to quantities that apply to a particular iteration and a particular sample. Note that the endmember misfit $\chi_{endmember}^2$ ignores the contribution of the hot-spring endmember because this endmember was picked from a uniform distribution. Similarly, $\left[\frac{Cl^-}{Ca^{2+}}\right]_{sil} = \left[\frac{Cl^-}{Ca^{2+}}\right]_{carb} = \left[\frac{Na^+}{Ca^{2+}}\right]_{carb} = 0$ (see Table 1), and these ratios are not considered in the

195 endmember misfit. The two misfits were then summed and weighted by the number of unique squared distances (three distances for χ_{splt}^2 – see equation 6 – and six distances for $\chi_{endmember}^2$ – see equation 7) to give equal weight to the summed sample and endmember misfits:

$$\chi_{total}^2 = \frac{\chi_{splt}^2}{3} + \frac{\chi_{endmember}^2}{6} \quad (9)$$

200 The choice of this weighting is arbitrary, and we tried some alternatives – the absence of any weighting does that do not change the results substantially. For each sample, the best fit set of endmembers and corresponding fractions, α_{Ca} , was then chosen from the iteration with the lowest total misfit. χ_{total}^2 were chosen as model output, whereas the uncertainty in these parameters was estimated based on from the standard deviation of all 100,000 Monte Carlo runs. We, excluding excluded those runs with reduced chi-squared distances of $\chi_{total}^2 > 1$ (~91% of runs) more than four (i.e. models with average distances of more than twice the uncertainty range of the input parameters).

205

Formatted: English (United States)

Formatted: English (United States)

The most important parameters in the mixing model are the endmember estimates (Table 1). Both, silicate and carbonate endmembers are based on compiled bedrock compositions around the study area (Chen et al., 2007; Jiang et al., 2018; Weller et al., 2013) (Table S3) as well as the assumption that: $\left[\frac{Cl^-}{Ca^{2+}}\right]_{sil} = \left[\frac{Cl^-}{Ca^{2+}}\right]_{carb} = \left[\frac{Na^+}{Ca^{2+}}\right]_{carb} = 0$. Published bulk rock analyses of rocks in the region show a substantial variability. Nevertheless, samples from the three individual lithologic groups

(granitoids, Paleozoic passive margin metapelites and Triassic flysch) form distinct trends in $Mg^{2+}/Ca^{2+} - Na^+/Ca^{2+}$ space (Fig. 3A-Ba-b). The composition of the granitoids varies around the global silicate endmember estimated from small streams that drain pure silicate lithologies (Burke et al., 2018; Gaillardet et al., 1999). Compared to the granites, the Paleozoic metapelites are substantially enriched in magnesium and the flysch rocks are characterized by high calcium contents (Fig. 3A-Ba-b). Major carbonate phases are not reported in the Paleozoic metapelites (Weller et al., 2013) and in the granitoids (Jiang et al., 2018).

Even if trace carbonate minerals can strongly affect solutes sourced from chemical weathering (Anderson et al., 2000; Blum et al., 1998; Emberson et al., 2016b; Jacobson and Blum, 2003), we assume that the bulk-rock geochemistry measurement are should be affected only negligibly. Thus, we assume that the mean and standard deviation of the bulk rock analyses compositions are dominated by and representative of the silicate endmember from these lithologies, and we use the mean and standard deviation of the elemental ratios from individual bedrock samples as an estimate for the silicate endmember of that bedrock group (Table 1). In turn, the flysch samples contain 4% – 80% carbonate that occurs both as calcite minerals and as carbonate cement (Chen et al., 2007). Therefore, these samples represent a mix between a carbonate and a silicate endmember (Fig. 3B3b). Based on two sediment samples with the highest carbonate content and zero sodium (Table S3), we estimated the magnesium content of carbonates in the area to $\left[\frac{Mg}{Ca}\right]_{br carb} = 0.038 \pm 0.006$ and $\left[\frac{Mg}{Ca}\right]_{br carb} = 0.023 \pm 0.004$ where subscript *br* denotes data from bedrock samples and the angle brackets denote the concentration in weight percent rather than in moles. This low ratio which is consistent with the absence of reported dolomite in the area (Chen et al., 2007). The error in this estimate is from the 68% confidence band of a regression through all flysch samples with a fixed intercept at $\left[\frac{Na^+}{Ca^{2+}}\right]_{sil} = 0$ and $\left[\frac{Mg^{2+}}{Ca^{2+}}\right]_{carb} = 0.04$ and assuming $\left[\frac{Mg^{2+}}{Ca^{2+}}\right]_{carb} \geq 0$ (Fig. A1B1b). Based on knowledge of the carbonate endmember, $\left[\frac{Mg}{Ca}\right]_{br carb}$ and $\left[\frac{Mg^{2+}}{Ca^{2+}}\right]_{carb}$, and the carbonate content of the samples $(Ca_{0.96}, Mg_{0.04})_{carb} CO_3$ (where square brackets denote the concentration in weight percent), the $\left[\frac{Na^+}{Ca^{2+}}\right]_{sil}$ and $\left[\frac{Mg^{2+}}{Ca^{2+}}\right]_{sil}$ ratios of the flysch is can be expressed as given

as:

$$\left[\frac{Na^+}{Ca^{2+}}\right]_{sil} = \frac{(Na)_{br sil}}{(Ca)_{br} - (Ca)_{br carb} \left(\frac{Ca}{Ca+Mg}\right)_{carb}} \frac{u_{Ca}}{u_{Na}} \quad (610)$$

and

$$\left[\frac{Mg^{2+}}{Ca^{2+}} \right]_{sil} = \frac{(Mg)_{br} - (Ca)_{br} \cdot \frac{(Mg)_{carb}}{(Ca)_{carb}}}{(Ca)_{br} - (Ca)_{carb}} \cdot \frac{u_{Ca}}{u_{Mg}} \quad (11)$$

where

$$\langle Ca \rangle_{carb} = \frac{(Ca_{0.96} Mg_{0.04} CO_3)_{br}}{u_{Ca} CO_3 + u_{Mg} CO_3} \cdot \frac{(Mg)_{carb}}{(Ca)_{carb}} \quad (7.12)$$

And u_X is the molar mass of component X (Bufe et al., 2021). We estimated $\left[\frac{Na^+}{Ca^{2+}} \right]_{sil}$ both ratios based on the assumption that the carbonate content of the bedrock flysch sample with the lowest carbonate content (farthest away from the origin along the regression in $\left[\frac{Na^+}{Ca^{2+}} \right] - \left[\frac{Mg^{2+}}{Ca^{2+}} \right]$ -space) has a carbonate content of $\langle Ca_{0.96} Mg_{0.04} CO_3 \rangle_{br} = 4-10$ wt%. The minimum value (4%) is from the lowest observed carbonate content in the field (Chen et al., 2007), whereas the upper bound is chosen so that the range of resulting $\left[\frac{Na^+}{Ca^{2+}} \right]_{sil}$ values reaches the global endmember value of $\left[\frac{Na^+}{Ca^{2+}} \right]_{sil} = 2.867$. We then used

an average of the resulting ratios $\left[\frac{Na^+}{Ca^{2+}} \right]_{sil}$ estimates with an uncertainty based on half of the range (e. The corresponding $\left[\frac{Mg^{2+}}{Ca^{2+}} \right]_{sil}$ was then deduced from $\left[\frac{Na^+}{Ca^{2+}} \right]_{sil}$ and the regression through the bedrock samples (Fig. 3a-b-A-B). Equivalently, the silicate endmember ratios normalized to Na for the forward model are:

$$\left[\frac{Ca^{2+}}{Na^+} \right]_{sil} = \frac{(Ca)_{br} - (Ca)_{carb}}{(Na)_{br}} \cdot \frac{u_{Na}}{u_{Ca}} \quad (13)$$

and

$$\left[\frac{Mg^{2+}}{Na^+} \right]_{sil} = \frac{(Mg)_{br} - (Ca)_{br} \cdot \frac{(Mg)_{carb}}{(Ca)_{carb}}}{(Na)_{br}} \cdot \frac{u_{Na}}{u_{Mg}} \quad (14)$$

We corrected all major elements for the cyclic endmember, we used a volume weighted average of atmospheric input using rainwater compositions from the eastern flank of Gongga Shan (Jiang et al., 2018) (Table 1, Table S4). The hot spring endmember is also based on hot spring compositions around Mt Gongga (Jiang et al., 2018) (Table S5). All hot springs are very distinct from rock samples, and notably characterized by $\left[\frac{Na^+}{Ca^{2+}} \right]$ -ratios that are 3 – 150-times higher than the highest measured stream water samples (Fig. 3A3a, Table S5). Nevertheless, hot spring compositions are highly variable, despite a relatively small area that was sampled (Fig. 3A3a). In the inversion, we therefore did not sample the hot spring endmembers from a

Formatted: Tab stops: 7 cm, Left

Formatted: English (United States)

normal distribution around a mean value. Instead, we picked $[Na^+]_{hs}$, $[Mg^{2+}]_{hs}$, and $[Ca^{2+}]_{hs}$ from uniform distributions that span the interquartile range of all hot spring samples. Because of a strong correlation between $[Cl^-]_{hs}$ and $[Na^+]_{hs}$ in these hot springs, we then picked $[Cl^-]_{hs}$ from the regression between $[Cl^-]_{hs}$ and $[Na^+]_{hs}$. ~~Moreover, we did not consider the hot spring endmember in finding the best fit model in the inversion.~~

As an alternative to the inverse model, we decomposed the data with a common forward approach (Bufe et al., 2021; Galy and France-Lanord, 1999; Jacobson and Blum, 2003; Meybeck, 1987; Moon et al., 2014). We assumed that all chloride in the river water samples was atmospherically derived and use precipitation-averaged $\left[\frac{x}{Cl^-}\right]_{cy}$ -ratios of the measured rainwater (Jiang et al., 2018) (Table S4) to adjust the sample concentrations for rain input. We assumed that our rainwater correction accounts for possible anthropogenic input of SO_4 from the industrialized Sichuan Basin through acid rain, and we neglected hot spring contributions. Then, the contributions of silicate and carbonate to the total dissolved Ca^{2+} and Mg^{2+} concentrations were estimated as:

$$[Ca^{2+}]_{sil, fw} = [Na^+]_{spt} \left[\frac{Ca^{2+}}{Na^+} \right]_{sil} \quad (8135)$$

$$[Mg^{2+}]_{sil, fw} = [Na^+]_{spt} \left[\frac{Mg^{2+}}{Na^+} \right]_{sil} \quad (9146)$$

$$[Ca^{2+}]_{carb, fw} = [Ca^{2+}]_{spt} - [Ca^{2+}]_{sil} \quad (40157)$$

$$[Mg^{2+}]_{carb, fw} = [Mg^{2+}]_{spt} - [Mg^{2+}]_{sil}$$

~~(1168).~~

Equivalent to the inverse model (equations 10 – 11) by the silicate endmember ratios for the flysch samples normalized to Na for the forward model were found by correcting for the carbonate content of the flysch bedrock samples are:

$$\left[\frac{Ca^{2+}}{Na^+} \right]_{sil} = \frac{(Ca)_{br} - (Ca)_{br, carb}}{(Na)_{br}} \frac{u_{Na}}{u_{Ca}} \quad (173)$$

and

$$\left[\frac{Mg^{2+}}{Na^+} \right]_{sil} = \frac{(Mg)_{br} - (Ca)_{br, carb} \frac{Mg}{Ca}}{(Na)_{br}} \frac{u_{Na}}{u_{Mg}} \quad (184)$$

280

3.3 Cation sums and fractions

The total sums of cations from silicate and carbonate weathering are:

$$C_{sil} = [Ca^{2+}]_{sil} + [Mg^{2+}]_{sil} + [Na^+] + [K^+] \quad (4219)$$

$$C_{carb} = [Ca^{2+}]_{carb} + [Mg^{2+}]_{carb} \quad (4320)$$

285 and in charge equivalents:

$$C_{sil}^{eq} = 2[Ca^{2+}]_{sil} + 2[Mg^{2+}]_{sil} + [Na^+] + [K^+] \quad (421)$$

$$C_{carb}^{eq} = 2[Ca^{2+}]_{carb} + 2[Mg^{2+}]_{carb} \quad (422)$$

The fraction of carbonate weathering is:

$$F_{carb} = \frac{C_{carb}^{eq}}{C_{carb}^{eq} + C_{sil}^{eq}} \quad (423)$$

290 The fraction of weathering by sulfuric acid (as opposed to carbonic acid) was estimated from sulfate concentrations (Bufe et al., 2021; Emberson et al., 2018; Galy and France-Lanord, 1999; Torres et al., 2016):

$$F_{sulf} = \frac{2[SO_4^{2-}]_w}{2[SO_4^{2-}]_w + [HCO_3^-]} \quad (424)$$

where $[SO_4^{2-}]_w$ is the sulfate concentration that is sourced from sulfide oxidation given by:

$$[SO_4^{2-}]_w = [SO_4^{2-}]_{spt} - [SO_4^{2-}]_{cy} - [SO_4^{2-}]_{hs} = [SO_4^{2-}]_{spt} - \alpha_{Ca,cy} \left[\frac{[SO_4^{2-}]}{[Ca^{2+}]} \right]_{cy} + \alpha_{Ca,hs} \left[\frac{[SO_4^{2-}]}{[Ca^{2+}]} \right]_{hs} \quad (425)$$

295 Note that this estimate of $[SO_4^{2-}]_w$ assumes that contributions of sulfate from evaporites are negligible in the area, and that any (likely minor) anthropogenic input [as well as minor salts associated with the metasedimentary rocks are](#) captured by the cyclic endmember measured in rainwater samples.

3.4 Estimate of denudation rate

Denudation rates were obtained from existing cosmogenic nuclide concentrations of *in situ*-produced ^{10}Be (Cook et al., 2018; 300 Ouimet et al., 2009). For two sampled catchments (S18.08 and S18.29) without previous denudation rate estimates, we processed two additional samples for analysis of *in situ* ^{10}Be following the procedure in Cook et al. (2018). Denudation rates were calculated using CRONUS scripts and the Lal/Stone scaling scheme with a sea-level low latitude nucleogenic production rate of 3.7 (Balco et al., 2008) (Table S6). These denudation rates integrate over the time denuding material resides in the first few upper meters of Earth surface. Although this integration time varies between catchments with different denudation rates, 305 it reflects the timescale of mineral supply to the weathering zone, and is therefore appropriate for comparison to weathering proxies. Where landslides dominate, their stochastic occurrence may disrupt the relationship between soil formation and chemical weathering (Emberson et al., 2016a; Emberson et al., 2016b) and may bias the denudation rate estimates (Chen et al., 2020; Niemi et al., 2005; Tofelde et al., 2018; Yanites et al., 2009). We assume that any such bias is within uncertainty of the denudation rate measurement. Cosmogenic-derived denudation rates incorporate both physical denudation and chemical 310 weathering, but physical denudation rates commonly greatly dominate denudation in active orogens uplifting siliceous rocks with minor carbonates, such as the ones described here (Dixon and von Blanckenburg, 2012; Erlanger et al., 2021; Gaillardet et al., 1999; Riebe et al., 2001; West et al., 2005). Thus, we assume that increasing denudation rates correspond to increasing

physical erosion rates. Finally, in situ ^{10}Be -derived denudation rates measure the denudation of quartz-containing bedrock. Based on published bedrock descriptions (Burchfiel et al., 1995; Chen et al., 2007; Jiang et al., 2018; Weller et al., 2013) and observations by the authors (Cook et al., 2018), we assume that carbonate and silicate phases in granitoids and metasediments are mixed to a degree that quartz-derived denudation rates approximate the denudation of the entire rock mass. We acknowledge that unquantified uncertainties may arise where significant weathering occurs below the top few meters of the regolith (Riebe and Granger, 2013), or where significant differences in quartz mineral contribution within the bedrock occur, but these uncertainties are unlikely to change the major trends observed in this work.

320 4 Results

In the studied catchments, the concentration of dissolved cations (TDC) generally increases with denudation rates (Fig. 4A4a). However, the strength of that relationship is greatly influenced by lithology (Fig. 4A4a). Whereas TDC increases 5 – 10-fold in the Triassic Songpan Ganze flysch, the increase of TDC with denudation in the granitic catchments is less than 2-fold and associated with substantial uncertainty (Spearman's $\rho = 0.19$) (Fig. 4A4a). Mixed flysch – granitic catchments fall in-between the two trends (Fig. 4A4a). Catchments with Paleozoic metamorphic lithologies have scattered TDC values, many of which fall within the range of values of the Triassic rocks (Fig. 4A4a). Magnesium and calcium dominate the solute load and constitute ~~42–42~~ – 96% (median 84.84%) of the TDC. The pattern of increasing TDC is dominated by an increase in calcium concentrations (Fig. 4B4b), whereas correlations between denudation rate and magnesium, sodium, and potassium concentrations are uncertain (Spearman's ρ values between 0.1 – 0.89) (Figs. 4C–E4c-e). Similarly, no relationship between chloride concentrations and denudation rates is evident (Fig. 4E4e), but sulfate concentrations show a strong increase with denudation rates in both granites and flysch lithologies (Fig. 4G4g).

The unmixed cation contributions follow the expectations from the raw data: Cation concentrations from carbonate weathering, C_{carb} , and sulfate from sulfide oxidation, $[\text{SO}_4^{2-}]_w$, display a strong relationship with denudation (Fig. 5A5a, Cc). In the flysch and in the Paleozoic metamorphics they increase rapidly-strongly with denudation rate, whereas the increase in the granitic catchments is weaker, and the mixed catchments are in-between (Fig. 5A5a, Cc). In contrast, cations from silicate weathering, precipitation sources, and hot springs generally show no relationship to denudation rate for any of the lithologies (Fig. 5B5b, Dd–Ee).

The contribution of carbonate weathering to the total solute load from weathering, F_{carb} , strongly increases with denudation irrespective of rock type (Fig. 6A6a). Even in granitic catchments carbonate weathering contributes ~~more than 50~~ 30 – % and ~~up to 89~~ 94% (median 65%) of the cation ~~charge concentration in most samples~~ (Fig. 6A6a). Thus, both granites and (meta)sedimentary lithologies have comparable fractions of carbonate weathering (Fig. 6A6a), even if the absolute concentrations differ (Fig. 4). The fraction of weathering by sulfuric acid, F_{sulf} , also increases with increasing denudation rate, although there is a large amount of scatter at higher denudation rates (Fig. 6B6b). ~~Importantly, F_{sulf} in the weakly~~

345 ~~metamorphosed flysch catchments appears relatively insensitive to denudation rate, whereas the higher grade metamorphic catchments have, on average, higher $F_{\text{sil}}/F_{\text{carb}}$ than the other lithologies. Granitic catchments have widely scattered $F_{\text{sil}}/F_{\text{carb}}$ values (Fig. 6B).~~

350 In ~~16–24~~ out of 35 samples (~~46–67~~% of samples), the inferred silicate and/or carbonate cation contributions differ by more than 20% between forward and inverse approaches (Fig. A2). For example, forward-modelled carbonate cation concentrations are more than 20% higher than results from the inversion in ~~10–11~~ samples (~~29–31~~% of samples) and more than 50% higher in 3 samples (9% of samples) (Fig. A2). Silicate cation concentrations inferred from the forward approach are lower in these samples. ~~All of~~ These samples lie outside of the zone formed between the silicate, carbonate, hot spring, and precipitation endmembers (Fig. 3b) which may explain the offset in the results. Conversely, ~~six–9~~ samples (~~17–26~~%) have more than 20% higher silicate cation concentrations inferred by the forward model (Fig. A2). In ~~all of~~ these samples, the inversion predicts ~~5–3–40–47~~% (median 13%) cation contributions from hot springs ~~whereas the median of the cation contributions from hot springs across all samples is 2%~~; The hot spring contribution is ignored in the forward approach, and all of the Na^+ is attributed to silicate instead, thereby leading to higher silicate cation contributions ~~in the forward model~~. Despite these differences and resulting outliers, the first order trends described in this contribution are unaffected by the choice of unmixing method (Figs. A3, A4).

360 Our concentration measurements cannot be converted into weathering fluxes, because we lack discharge or runoff data for the sampled catchments. However, in comparison to the nearly three-orders-of-magnitude-wide denudation gradient, the mean annual precipitation does not vary widely across the catchments: 82% of the catchments differ by less than a factor of two and 90% by less than a factor of three of precipitation (Table S1). Further, there is no co-variation between precipitation and denudation rate (Fig. ~~2B2b~~, Table S1). ~~Finally, The first-order patterns described above do not change substantially when we consider “the observed first-order patterns described above do not change substantially when we estimate inferred” weathering fluxes that are obtained by using mean annual precipitation values as a proxy for runoff (Fig. A5). Therefore, it is unlikely that differences in runoff between catchments strongly affect our data, and Therefore, we interpret the observed patterns as reflecting the response of the weathering system to changes in denudation we assume that the measured concentrations scale with weathering fluxes from these catchments.~~

5 Discussion

370 Our analysis indicates that increasing denudation rates lead to an increase in carbonate weathering and sulfide oxidation in all sampled lithologies (Figs. 5-6), likely due to the increased supply of carbonate and sulfide minerals during erosion (Bufe et al., 2021; Calmels et al., 2007; Torres et al., 2016). Conversely, silicate weathering appears to be insensitive to denudation rate and represent a small proportion of the total weathering budget (Figs. 5-6). While the granitic catchments have systematically lower cation concentrations from carbonate weathering than the metasedimentary catchments (Fig. ~~5A5a~~), the fraction of

375 carbonate weathering (F_{carb}) is increasing with denudation and is of similar magnitude in all rock-types (Fig. 6A6a). Even in
catchments underlain by granitoid rocks, weathering of carbonate phases dominates the solute load at denudation rates above
0.1 mm/yr (Fig. 6A6a). This finding likely arises from the dissolution of trace carbonate minerals disseminated in the crustal
granitoids and metapelites that has been described in a number of active mountain ranges (Blum et al., 1998; Bufe et al., 2021;
Emberson et al., 2017; Jacobson et al., 2003; Torres et al., 2016; White et al., 1999). In turn, the insensitivity of silicate cation
380 concentrations to denudation (Fig. 5B5b) is consistent with a kinetic limitation of silicate weathering (Gabet and Mudd, 2009;
West, 2012; West et al., 2005). Such kinetic limitation of silicate weathering in conjunction with increasing sulfide oxidation
and carbonate weathering across multiple orders of magnitudes of denudation rates (Fig. 5) has recently been documented in
the low-grade metasedimentary rocks of southern Taiwan (Bufe et al., 2021). The data presented here suggest that this pattern
applies to metasediments in another mountain range, as well as to granitoid rocks. A series of studies on soil formation in
385 metasedimentary and granitic rocks ~~across erosiondenudation rates from 10⁻³ mm/y to 2 mm/y~~ has suggested a link between
soil denudation rates and soil production rates, and this sensitivity of soil formation rates to denudation has been used to argue
for a relationship between orogenesis and silicate weathering (Dixon et al., 2012; Dixon and von Blanckenburg, 2012; Larsen
et al., 2014; Riebe et al., 2004; Riebe et al., 2001). ~~In contrast, our data that spans~~Spanning a comparable range of
~~erosiondenudation rates, our data~~ confirm that these findings from soil profiles may not directly translate to the catchment
390 scale (Dixon and von Blanckenburg, 2012; West et al., 2005). ~~This disconnect is~~due, most likely, to the ~~dissolution-dilution~~
of soil waters by fluids ~~from that drain parts of the landscape that are not soil-covered~~soil-free parts of the landscape or other
~~parts of the landscape~~follow deep pathways through bedrock. For example, mass movements, such as landslides, that dominate
~~erosion in parts of the study area—such as landslides, are expected to alter weathering fluxes~~ (Emberson et al., 2016a). Thus,
in active mountain ranges, landscape-scale silicate weathering may be largely insensitive to denudation rates independently of
395 the major lithologies (Bufe et al., 2021; Gabet and Mudd, 2009; West, 2012).

Even though yearly average precipitation rates do not vary considerably across the denudation rate gradient, monthly
precipitation can vary by a factor of ~5 – 6 between the high- and low-flow seasons (Jiang et al., 2018). Nevertheless, in small
catchments around Mount Gongga, the total dissolved cation concentrations of 80% of rivers is diluted by less than two-fold
in the high-flow season (median 1.3-fold) and only Cl⁻ and Mg²⁺ show substantial dilution (Jiang et al., 2018). Thus, the
400 patterns of concentrations that we described here should broadly mirror the differences in annual weathering fluxes between
catchments. Solute concentrations during the high-flow season are expected to carry an elevated proportion of carbonate
weathering with respect to the low flow season (Kemeny et al., 2021; Tipper et al., 2006). Thus, by sampling during the low
flow season, and by not accounting for cation exchange with suspended sediment from the clay minerals (Tipper et al., 2021),
we might overestimate the proportion of silicate weathering (Kemeny et al., 2021; Tipper et al., 2006; Tipper et al., 2021). The
405 dominance of carbonate weathering over silicate weathering in all catchments (Fig. 6) would, therefore, most likely be
strengthened with more data across all seasons and/or with suspended sediment data.

Formatted: Superscript

The sulfuric-acid-derived sulfate concentrations $[SO_4^{2-}]_w$ and the cation concentrations from silicate weathering allow to estimate the concentration of CO_2 that is sequestered or emitted during chemical weathering (Emberson et al., 2018; Torres et al., 2016). Beyond the calcium carbonate compensation time (of ~10 ky; (Zeebe and Westbroek, 2003)^{ref62}), the moles of CO_2 produced (positive $[CO_2]$) or sequestered (negative $[CO_2]$) during chemical weathering per unit volume of weathering fluid can be expressed as:

$$[CO_2] = [SO_4^{2-}]_w^{eq} - 0.5 C_{carb\&sil}^{eq} \quad (4923)$$

(Bufe et al., 2021; Torres et al., 2016) (see supplement of Torres et al., 2016) (Fig. 5A) (Table S7). Note that this formulation is independent of the proportion of sulfuric acid that weathers carbonates or silicates (see supplement of Torres et al., 2016).

The increase of F_{carb} and F_{sulf} with denudation rate (Fig. 6) leads to a clear change from CO_2 sequestration to CO_2 release (Fig. 7A). These observed trends are most likely explained by the combination of a supply limitation on coupled pyrite oxidation and carbonate weathering and a limitation of silicate weathering rates by the slow dissolution kinetics of silicate minerals (Bufe et al., 2021; Calmels et al., 2007; Gabet and Mudd, 2009; Torres et al., 2016). Fifteen catchments fall into the long-term CO_2 release field including all of the metamorphic catchments (Paleozoic and Triassic), four of the granitoid catchments, and three mixed granitic/metamorphic catchments (Fig. 7). All of these catchments have denudation rates above 0.19 mm/yr. However, increasing denudation rates, even in granitoid rocks, lead to decreases in the proportion of weathering that contributes to CO_2 drawdown, as sulfate concentrations increase, while silicate cation concentrations are invariable (Figs. 4-6).

Compared to the other lithologies, water samples from granite catchments have substantially lower solute concentrations than waters from (meta)sedimentary catchments and weathering in granitoid catchments remains closest to the CO_2 consumption field across the entire denudation rate gradient (Fig. 7A), largely due to lower sulfate concentrations (Fig. 5C). However, increasing denudation rates, even in granitoid rocks, lead to decreases in the proportion of weathering that contributes to CO_2 drawdown, as sulfate concentrations increase, while silicate cation concentrations are invariable (Figs. 4-6).

This contrast persists when we consider “inferred” weathering fluxes that are obtained using mean annual precipitation values as a proxy for runoff (Fig. A5d). In the absence of major differences in climate or topography between granitic and metasedimentary catchments (Fig. 2), this contrast in concentrations is most likely due to low proportions of minor carbonate and sulfide phases in the granitoid lithologies. In this case, variations in lithology may change the flux of CO_2 by a factor of 5 – 10; a change that is approximately equivalent to an order of magnitude variation in the denudation rates of metasedimentary rocks (Fig. 7, A5d). Hence, even if the relative pattern of silicate, sulfide, and carbonate weathering are similar across all lithologies, the absolute weathering fluxes are not. As a consequence, our data suggest that changes in the exposed lithologies

Formatted: French (France)

Formatted: French (France)

Field Code Changed

Formatted: French (France)

Formatted: English (United Kingdom)

Field Code Changed

Formatted: English (United Kingdom)

Formatted: Subscript

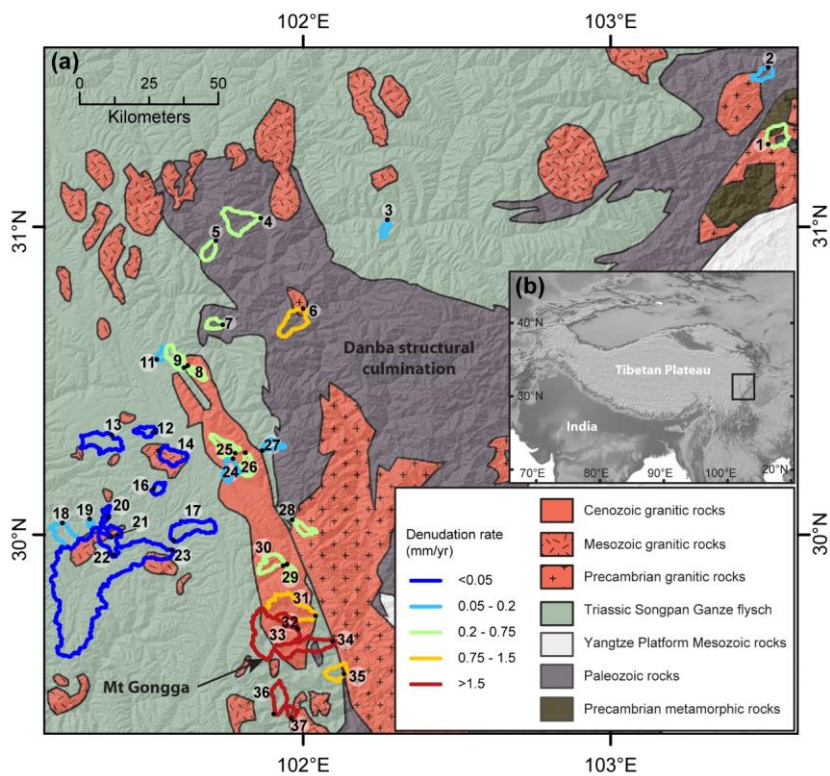
across an orogenic cycle can substantially alter weathering fluxes (up to a factor of 5 – 10) independently of variations in denudation rates or runoff.

440 Catchments with metamorphosed flysch as well as those with metamorphic Paleozoic sediments (marked by black dots in all data figures) show the highest tendency toward weathering pathways that release CO₂, and they have the highest $[SO_4^{2-}]_w$ (Fig. 7B). Assuming that sulfide oxidation is limited by the supply of sulfides to the weathering zone (Bufe et al., 2021; Calmels et al., 2007; Torres et al., 2016), we expect a linear increase of sulfate concentrations with denudation (assuming constant runoff). A linear regression of the relationship between sulfate concentration and denudation rate for
445 unmetamorphosed Triassic flysch samples has a gentler slope than a regression through all metapelites, although the scatter in the data leads to overlap in the confidence bands (Fig. 7B). Whereas most of the metamorphic catchments are Paleozoic metapelites, two samples come from metamorphosed Triassic flysch, and they follow the steeper trend of the metamorphic catchments (Fig. 7B). These first data suggest that metamorphism could increase the sulfide content available for oxidation. The production of sulfide by thermal reduction of trace marine sulfates embedded in marine sediments becomes efficient at
450 temperatures above ~500 °C (Goldstein and Aizenshtat, 1994), and could be a viable explanation. The process of metamorphism may therefore alter the balance of weathering pathways and promote CO₂ release once rocks reach the surface, with implications for the evolution of weathering fluxes across the development of an orogen.

6 Conclusion

Water chemistry data from catchments on the eastern margin of the Tibetan plateau that span across three orders of magnitude
455 in denudation rate illustrate the role of lithology in modulating the link between denudation rate and chemical weathering. Perhaps surprisingly, our data show a uniformity in the first-order relationships between weathering and denudation between different lithologies. In particular, in all lithologies, silicate cation concentrations do not increase with increasing denudation rates whereas concentrations of sulfate and of cations from carbonate do show an increase. Whereas granitic and (meta)sedimentary rocks are characterized by similar fractions of carbonate weathering that are increasing with denudation
460 rate, the (meta)sediments have higher absolute concentrations of sulfate and of cations from carbonate weathering, likely due to higher concentrations of these minor phases in the bedrock. In combination, the weathering reactions lead to a transition from CO₂ drawdown to CO₂ release at denudation rates >higher than 0.2 mm/yr, even in granitic catchments. In turn, absolute weathering fluxes can vary by a factor of 5 – 10 between catchments draining granites and (meta)sediments with implications for the role of changes in the relative exposure of igneous and sedimentary rocks during mountain growth. Our data also
465 suggest, albeit with large uncertainties, that the contribution of sulfuric acid to weathering from a given lithology can be increased due to metamorphism of that rock type. Consequently, as mountain belts mature and denudation exposes more deeply buried rocks, weathering pathways may increasingly trend towards CO₂ release at high denudation rates.

Figures



470

Figure 1: Overview of the study area

(a) Simplified geologic map of the study area showing sample locations, sample numbers, and catchment outlines. Outline color indicates ^{10}Be basin-wide denudation rate from Cook et al. (2018), with two samples from this study (Table S6). (b) Location of study area.

475

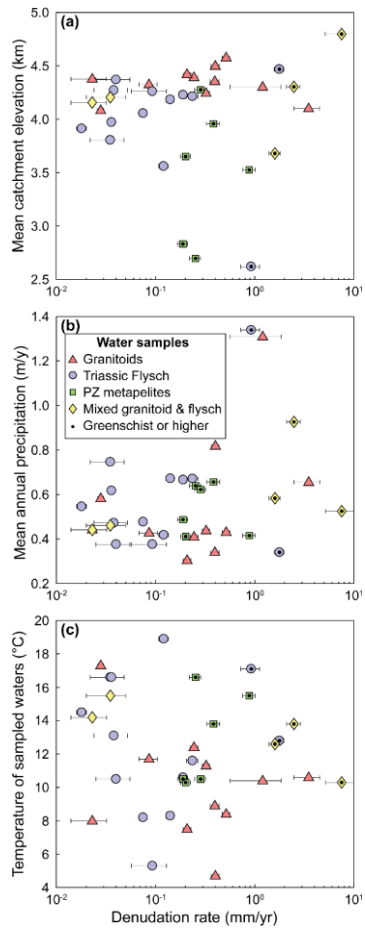


Figure 2: Variability of topographic and climatic parameter across the denudation gradient

(a) Catchment-averaged elevation upstream of each sample as a function of denudation rate. (b) TRMM-derived mean annual precipitation in the catchment as a function of denudation rate. (c) Temperature of sampled waters as a function of denudation rate. Catchments underlain by different lithologies are distinguished by symbols and color. Datapoints with a black dot are metamorphosed to greenschist facies or higher.

480

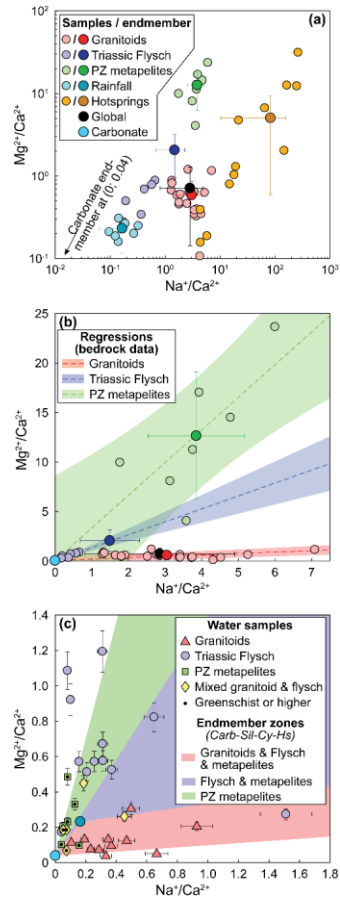


Figure 3: Endmembers and mixing lines in $\text{Na}^+/\text{Ca}^{2+}$ – $\text{Mg}^{2+}/\text{Ca}^{2+}$ space

485 (a) Small points mark individual bedrock, rain water, and hot spring chemistry (Table S3) (Chen et al., 2007; Jiang et al., 2018; Weller et al.,
 2013). Large points with error bars mark corresponding endmember estimates (Table 1). Silicate endmembers for granitoids and Paleozoic
 metamorphics as well as for the rainfall endmember are estimated from a mean and standard deviation of individual datapoints. The flysch
 silicate endmember was derived from a regression through the bedrock data and estimates of the carbonate content in the bedrock flysch
 samples (see text). For hot springs, the endmember is the median and interquartile range. The carbonate endmember cannot be shown in
 490 logarithmic space. (b) Bedrock chemistry and endmembers with mixing lines between silicate and carbonate endmembers regressions through
the bedrock data. Colored circle without error bars are lithology data. Colored points with error bars mark the estimate for the silicate

endmember for each lithology. Light Grey/blue point marks carbonate endmember. (c) Individual water samples within the endmember space. Colored areas mark the space between the carbonate, silicate, precipitation, and hot spring endmembers for each lithology. Note that spaces are overlapping. Catchments underlain by different lithologies are distinguished by symbols and color. Datapoints with a black dot are metamorphosed to greenschist facies or higher.

495

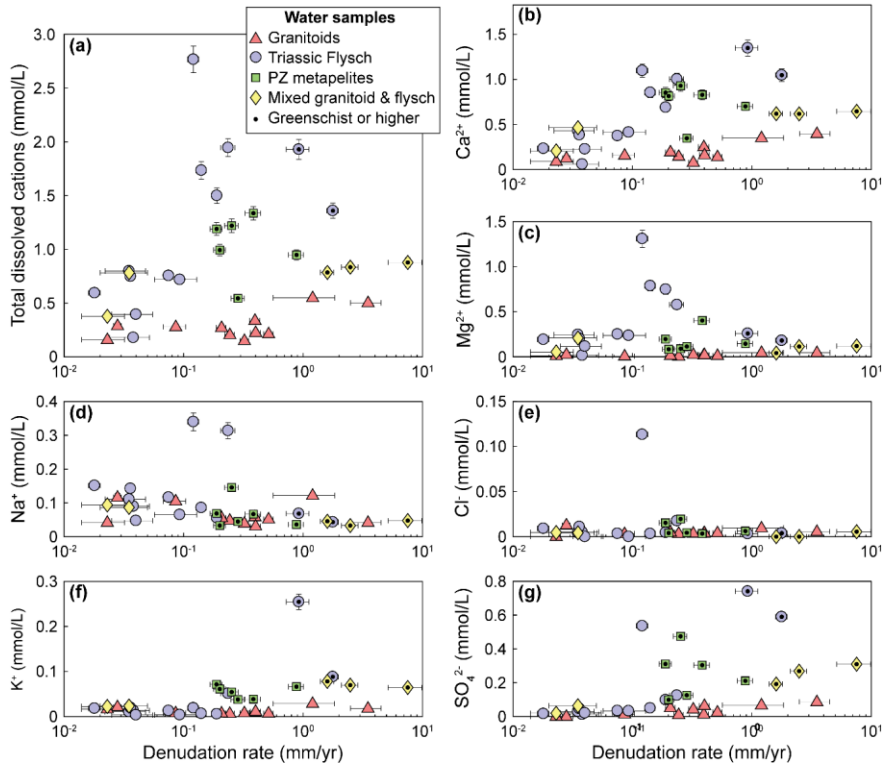


Figure 4: Solute concentrations vs. denudation rate

(a) Total dissolved cations. Spearman's rank correlation coefficient and associated p-value: $\rho_{granite}^{TDCS} = 0.43$, $p_{granite}^{TDCS} = 0.19$;

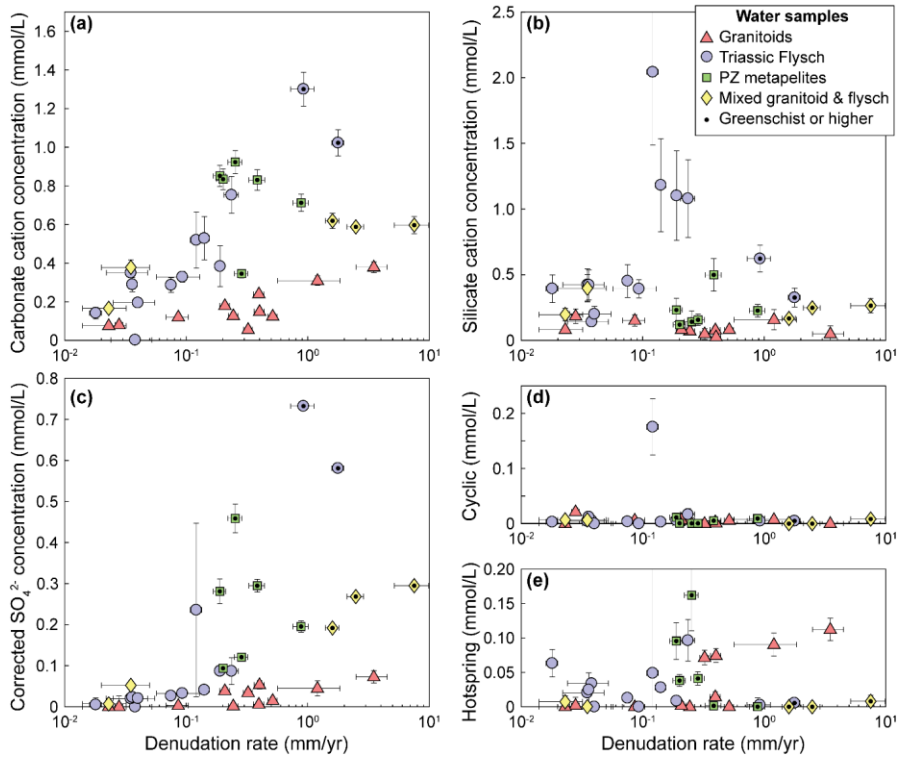
500

$\rho_{flysch}^{TDC} = 0.693$, $p_{flysch}^{TDC} = 0.013$. (Bb) Ca^{2+} concentrations $\rho_{granite}^{Ca^{2+}} = 0.623$, $p_{granite}^{Ca^{2+}} = 0.04$; $\rho_{flysch}^{Ca^{2+}} = 0.773$, $p_{flysch}^{Ca^{2+}} =$

0.00603 . (Cc) Mg^{2+} concentrations. (Dd) Na^+ concentrations. (Ee) K^+ concentrations. (Ff) Cl^- concentrations. (Gg) SO_4^{2-} concentrations

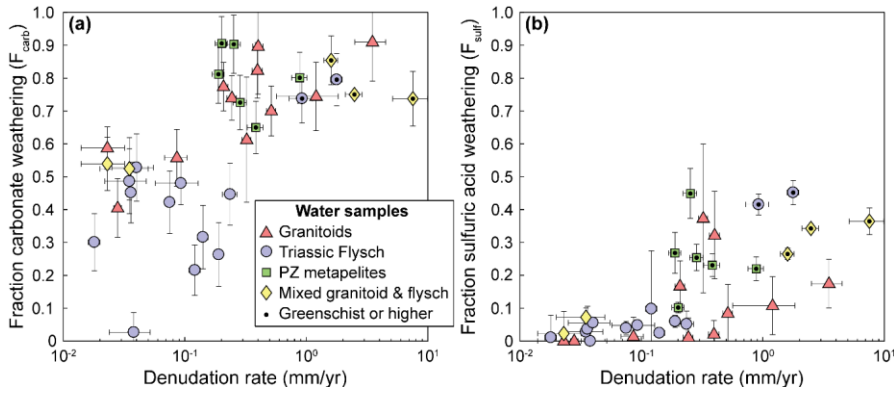
$\rho_{granite}^{SO_4^{2-}} = 0.820$, $p_{granite}^{SO_4^{2-}} = 0.0023$; $\rho_{flysch}^{SO_4^{2-}} = 0.9376$, $p_{flysch}^{SO_4^{2-}} = < 0.0024$. Catchments underlain by different lithologies are

distinguished by symbols and color. Datapoints with a black dot are metamorphosed to greenschist facies or higher.



505 **Figure 5: Unmixed contributions to the solute load**

(a) Cation concentrations from carbonate weathering. (b) Cation concentrations from silicate weathering. (c) Sulfate concentrations corrected for precipitation and inferred to derive from sulfide oxidation. (d) Cation concentrations from precipitation-cyclic sources. (e) Cation concentrations from hot spring sources. Catchments underlain by different lithologies are distinguished by symbols and color. Datapoints with a black dot are metamorphosed to greenschist facies or higher.



510

Figure 6: Fraction of carbonate weathering and weathering by sulfuric acid

(a) Fraction of carbonate weathering (eq. 1623). (b) Fraction of weathering by sulfuric acid (eq. 1724). Symbols indicate catchment lithology. Catchments underlain by different lithologies are distinguished by symbols and color. Datapoints with a black dot are metamorphosed to greenschist facies or higher.

515

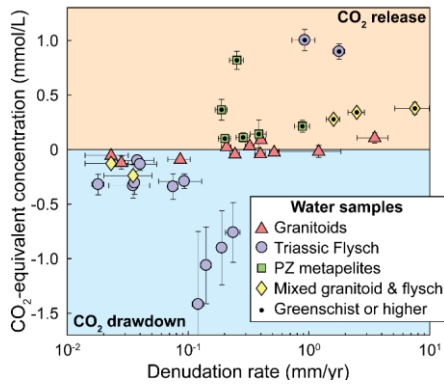


Figure 7: Influence of weathering on the carbon cycle

(a) Equivalent concentration of CO₂ released or consumed. (b) Sulfate from sulfide oxidation with linear regressions (curved due to semi-log plot). Blue regression is through only the unmetamorphosed flysch. Black regression is through all of the Triassic flysch and Paleozoic metamorphic rocks. Symbols indicate catchment lithology. Catchments underlain by different lithologies are distinguished by symbols and color. Datapoints with a black dot are metamorphosed to greenschist facies or higher.

520

Formatted: Centered

Table 1. Input endmembers for mixing model

Endmember	Na/Ca	±Na/Ca	Mg/Ca	±Mg/Ca	Cl/Ca	±Cl/Ca
Silicate: Granite	2.78	1.53	0.59	0.28	0	0
Silicate: Paleozoic metapelites	3.76	1.32	11.24	6.42	0	0
Silicate: Flysch	1.46	0.77	1.95	1.00	0	0
Silicate: Global	2.86	2.04	0.71	0.57	0	0
Carbonate	0	0	0.04	0.13	0	0
Precipitation	0.16	0.12	0.23	0.11	0.98	0.47

Formatted Table

Table 1. Input endmembers for mixing model

Endmember	Na/Ca	±Na/Ca	Mg/Ca	±Mg/Ca	Cl/Ca	±Cl/Ca	Ca/Na	±Ca/Na	Mg/Na	±Mg/Na
Silicate: Granite	3.05	1.53	0.59	0.28	0	0	0.41	0.20	0.25	0.19
Silicate: Paleozoic metapelites	3.85	1.32	12.65	6.42	0	0	0.29	0.13	3.38	1.43
Silicate: Flysch	1.49	0.81	2.06	1.10	0	0	0.72	0.34	1.31	0.01
Silicate: Global	2.86	2.04	0.71	0.57	0	0	0.35	0.25	0.25	0.20
Carbonate	0	0	0.038	0.006	0	0	-	-	-	-
Cyclic	0.17	0.1	0.23	0.12	0.98	0.41	-	-	-	-
	Na/Ca	Na/Ca	Mg/Ca	Mg/Ca	Cl/Ca	Cl/Ca	-	-	-	-
Hotspring	Q1*	Q3**	Q1*	Q3**	Q1*	Q3**				
	10	156	0.6	9.5	2.6	50.6	-	-	-	-

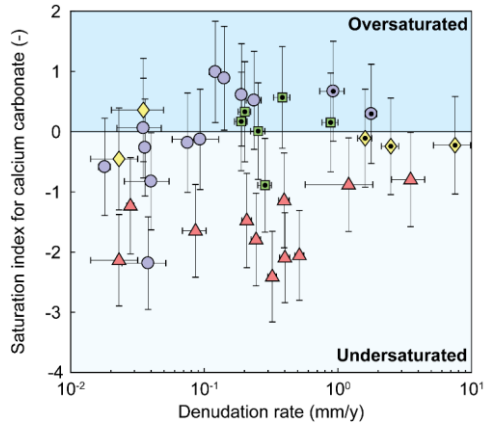
*First quartile

Formatted: Font: 8 pt

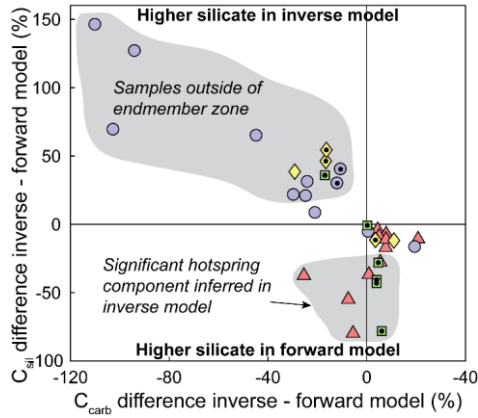
**Second quartile

Formatted: Font: 8 pt

Appendix A: Supporting figures



530 **Figure A1: Saturation index of samples with respect to calcium carbonate**
 Catchments underlain by different lithologies are distinguished by symbols and color. Datapoints with a black dot are metamorphosed to greenschist facies or higher.



535 **Figure A2: Difference between forward and inverse unmixing approaches**
 Positive values indicate that the inverse approach predicts higher cation ratios than the forward approach. All samples in the upper left quadrant are outside of the carbonate – silicate – hotspring – precipitation endmember space in $\text{Na}^+/\text{Ca}^{2+} - \text{Mg}^{2+}/\text{Ca}^{2+}$ space (Fig. 3E3E).

The five samples with lower inverse silicate cation concentrations are characterized by >53-47% hot spring contribution that is not accounted for in the forward model (see text). Catchments underlain by different lithologies are distinguished by symbols and color.

540 Datapoints with a black dot are metamorphosed to greenschist facies or higher.

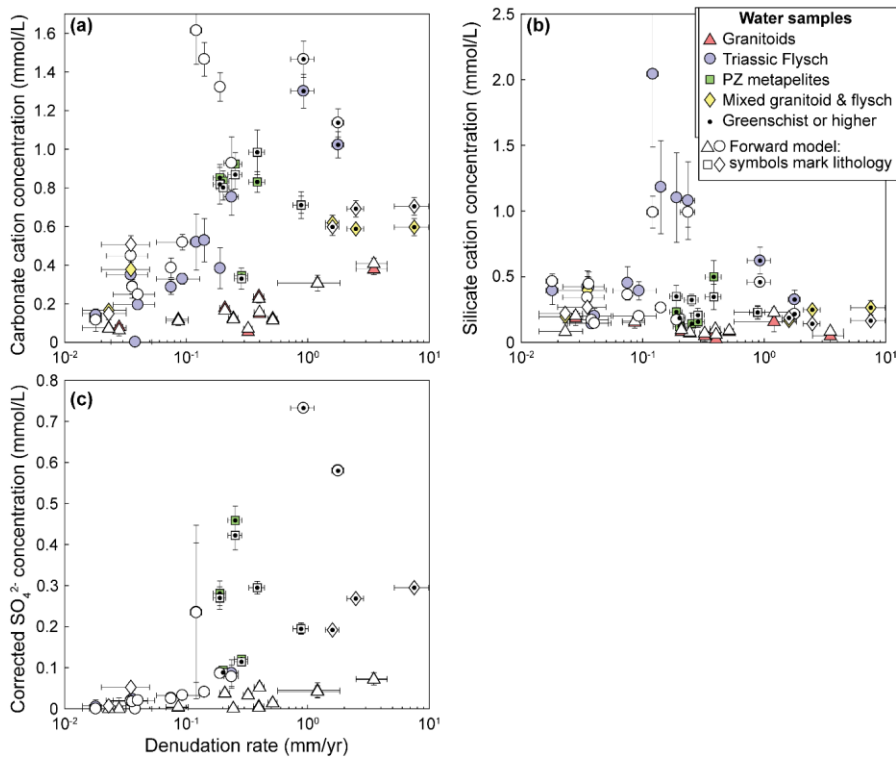


Figure A3: Forward model results for silicate, carbonate, and sulfide weathering contributions

Data from Fig. 5 plotted with results from the forward model (white points). Lithology in the data from the forward model is

545 distinguished by symbology only. Where results from forward and inverse approaches are similar, symbols overlap.

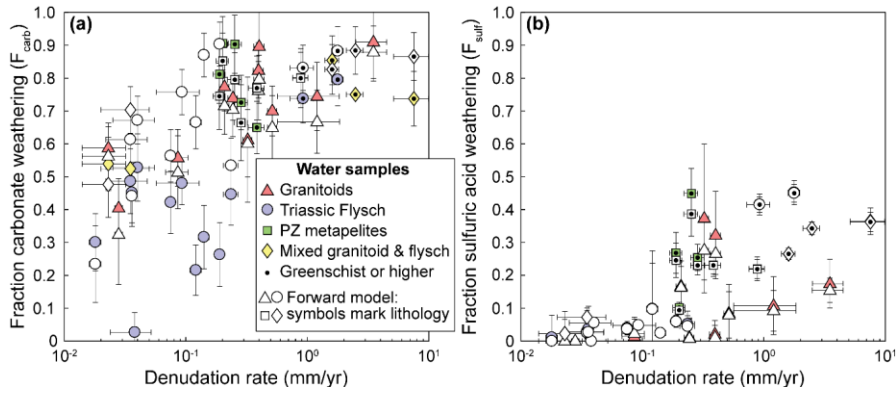


Figure A4: Forward model results for the fraction of carbonate weathering and weathering by sulfuric acid

Data from Fig. 6 plotted with results from the forward model (white points). Lithology in the data from the forward model is distinguished by symbology only. Where results from forward and inverse approaches are similar, symbols overlap.

550

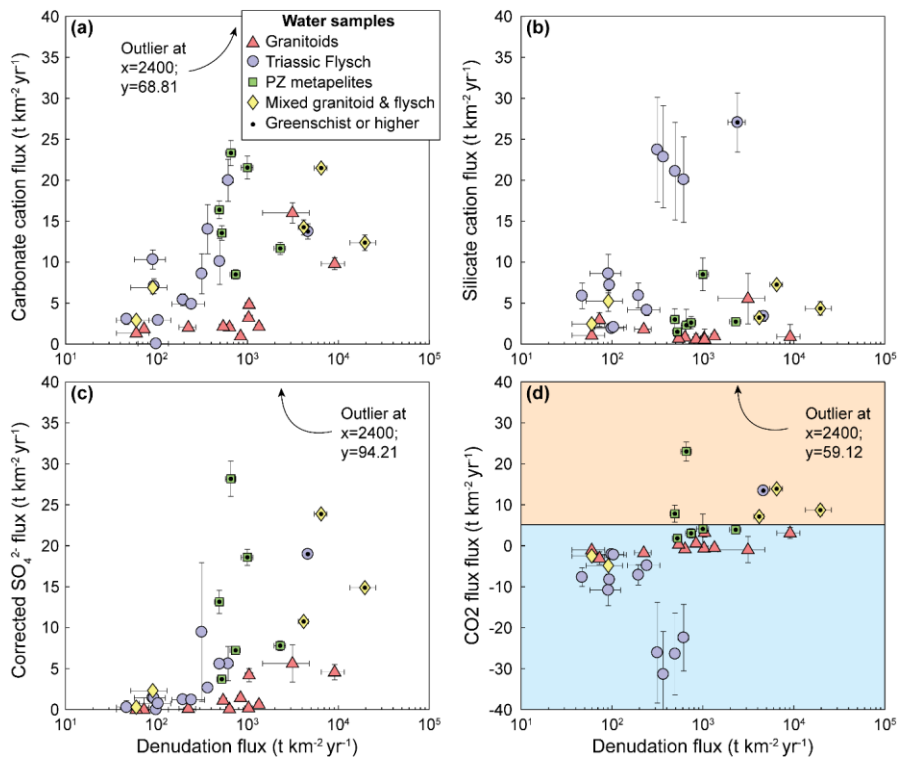


Figure A5: Inferred weathering fluxes

(a-c) Data from Fig. 5a-c and (d) data from Fig. 7 converted to fluxes by using mean annual precipitation as runoff estimate. One outlier with exceptional precipitation values is not plotted on panels a,b, and d.

Data Availability

All data used in this paper are included as tables in the Supplement.

Author contribution

560 K.L.C. and N.H. conceived the study and collected samples in the field. A.B., H.W., and A.G. contributed to laboratory analyses. K.L.C. and A.B. led the data analysis and interpretation and wrote the manuscript with input from all authors.

Competing interest

The authors declare that they have no conflict of interest.

Acknowledgements

565 We thank Fan Xuanmei and Chen Jie for help with fieldwork logistics. Bernhard Zimmermann, Jutta Schlegel, Daniel Frick, Andrea Gottsche, Tanya Goldberg, and the HELGES Lab are thanked for laboratory assistance. [We thank J. Jotautas Baronas and an anonymous reviewer for detailed and constructive comments on an earlier version of the manuscript.](#)

Financial support

570 AB has received funding from the European Union's Horizon 2020 research and innovation programme under the Marie Skłodowska-Curie grant agreement No 841663.

References

- Anderson, S. P., Drever, J. I., Frost, C. D., and Holden, P., 2000, Chemical weathering in the foreland of a retreating glacier: *Geochimica et Cosmochimica Acta*, v. 64, no. 7, p. 1173-1189.
- 575 Balco, G., Stone, J. O., Lifton, N. A., and Dunai, T. J., 2008, A complete and easily accessible means of calculating surface exposure ages or erosion rates from ¹⁰Be and ²⁶Al measurements: *Quaternary Geochronology*, v. 3, no. 3, p. 174-195.
- Berner, R. A., 1978, Rate control of mineral dissolution under Earth surface conditions: *American Journal of Science*, v. 278, no. 9, p. 1235-1252.
- Berner, R. A., Lasaga, A. C., and Garrels, R. M., 1983, The carbonate-silicate geochemical cycle and its effect on atmospheric carbon dioxide over the past 100 million years: *American Journal of Science*, v. 283, no. 7, p. 641-683.
- 580 Blattmann, T. M., Wang, S. L., Lupker, M., Märki, L., Haghypour, N., Wacker, L., Chung, L. H., Bernasconi, S. M., Plötze, M., and Eglinton, T. I., 2019, Sulphuric acid-mediated weathering on Taiwan buffers geological atmospheric carbon sinks: *Scientific Reports*, v. 9, no. 1, p. 2945.
- Blum, J. D., Gazis, C. A., Jacobson, A. D., and Page Chamberlain, C., 1998, Carbonate versus silicate weathering in the Raikhot watershed within the High Himalayan Crystalline Series: *Geology*, v. 26, no. 5, p. 411-414.
- 585 Bookhagen, B., and Burbank, D. W., 2010, Toward a complete Himalayan hydrological budget: Spatiotemporal distribution of snowmelt and rainfall and their impact on river discharge: *Journal of Geophysical Research: Earth Surface*, v. 115, no. F3, p. F03019.
- Bufe, A., Hovius, N., Emberson, R., Rugenstein, J. K. C., Galy, A., Hassenruck-Gudipati, H. J., and Chang, J.-M., 2021, Co-variation of silicate, carbonate and sulfide weathering drives CO₂ release with erosion: *Nature Geoscience*, v. 14, no. 4, p. 211-216.
- 590 Burchfiel, B. C., Zhiliang, C., Yupinc, L., and Royden, L. H., 1995, Tectonics of the Longmen Shan and Adjacent Regions, Central China: *International Geology Review*, v. 37, no. 8, p. 661-735.
- Burke, A., Present, T. M., Paris, G., Rae, E. C. M., Sandilands, B. H., Gaillardet, J., Peucker-Ehrenbrink, B., Fischer, W. W., McClelland, J. W., Spencer, R. G. M., Voss, B. M., and Adkins, J. F., 2018, Sulfur isotopes in rivers: Insights into global weathering budgets, pyrite oxidation, and the modern sulfur cycle: *Earth and Planetary Science Letters*, v. 496, p. 168-177.
- 595 Calmels, D., Gaillardet, J., Brenot, A., and France-Lanord, C., 2007, Sustained sulfide oxidation by physical erosion processes in the Mackenzie River basin: Climatic perspectives: *Geology*, v. 35, no. 11, p. 1003-1006.
- Caves Rugenstein, J. K., Ibarra, D. E., and von Blanckenburg, F., 2019, Neogene cooling driven by land surface reactivity rather than increased weathering fluxes: *Nature*, v. 571, no. 7763, p. 99-102.
- Chen, C.-Y., Willett, S. D., West, A. J., Dadson, S., Hovius, N., Christl, M., and Shyu, J. B. H., 2020, The impact of storm-triggered landslides on sediment dynamics and catchment-wide denudation rates in the southern Central Range of Taiwan following the extreme rainfall event of Typhoon Morakot: *Earth Surface Processes and Landforms*, v. 45, no. 3, p. 548-564.
- 600 Chen, Y., Liu, F., Zhang, H., Nie, L., and Jiang, L., 2007, Elemental and Sm-Nd isotopic geochemistry on detrital sedimentary rocks in the Ganzi-Songpan block and Longmen Mountains: *Frontiers of Earth Science in China*, v. 1, no. 1, p. 60.
- Cook, K. L., Hovius, N., Wittmann, H., Heimsath, A. M., and Lee, Y.-H., 2018, Causes of rapid uplift and exceptional topography of Gongga Shan on the eastern margin of the Tibetan Plateau: *Earth and Planetary Science Letters*, v. 481, p. 328-337.
- 605 Das, A., Chung, C.-H., and You, C.-F., 2012, Disproportionately high rates of sulfide oxidation from mountainous river basins of Taiwan orogeny: Sulfur isotope evidence: *Geophysical Research Letters*, v. 39, no. 12, p. L12404.
- Dessert, C., Dupré, B., Gaillardet, J., François, L. M., and Allègre, C. J., 2003, Basalt weathering laws and the impact of basalt weathering on the global carbon cycle: *Chemical Geology*, v. 202, no. 3, p. 257-273.
- 610 Dixon, J. L., Chadwick, O. A., and Vitousek, P. M., 2016, Climate-driven thresholds for chemical weathering in postglacial soils of New Zealand: *Journal of Geophysical Research: Earth Surface*, v. 121, no. 9, p. 1619-1634.
- Dixon, J. L., Hartshorn, A. S., Heimsath, A. M., DiBiase, R. A., and Whipple, K. X., 2012, Chemical weathering response to tectonic forcing: A soils perspective from the San Gabriel Mountains, California: *Earth and Planetary Science Letters*, v. 323-324, p. 40-49.
- Dixon, J. L., and von Blanckenburg, F., 2012, Soils as pacemakers and limiters of global silicate weathering: *Comptes Rendus Geoscience*, v. 344, no. 11-12, p. 597-609.
- 615 Drever, J. I., and Clow, D. W., 2018, Weathering Rates in Catchments, *in* White, A. F., and Brantley, S. L., eds., *Chemical Weathering Rates of Silicate Minerals*, De Gruyter, p. 463-484.
- Drever, J. I., and Zobrist, J., 1992, Chemical weathering of silicate rocks as a function of elevation in the southern Swiss Alps: *Geochimica et Cosmochimica Acta*, v. 56, no. 8, p. 3209-3216.
- 620 Emberson, R., Galy, A., and Hovius, N., 2017, Combined effect of carbonate and biotite dissolution in landslides biases silicate weathering proxies: *Geochimica et Cosmochimica Acta*, v. 213, p. 418-434.
- , 2018, Weathering of Reactive Mineral Phases in Landslides Acts as a Source of Carbon Dioxide in Mountain Belts: *Journal of Geophysical Research: Earth Surface*, v. 123, no. 10, p. 2695-2713.
- Emberson, R., Hovius, N., Galy, A., and Marc, O., 2016a, Chemical weathering in active mountain belts controlled by stochastic bedrock landsliding: *Nature Geoscience*, v. 9, no. 1, p. 42-45.

- 625 Emberson, R., Hovius, N., Galy, A., and Marc, O., 2016b, Oxidation of sulfides and rapid weathering in recent landslides: *Earth Surf. Dynam.*, v. 4, no. 3, p. 727-742.
- Erlanger, E. D., Rugenstein, J. K. C., Bufer, A., Picotti, V., and Willett, S. D., 2021, Controls on Physical and Chemical Denudation in a Mixed Carbonate-Siliciclastic Orogen: *Journal of Geophysical Research: Earth Surface*, v. n/a, no. n/a, p. e2021JF006064.
- 630 Gabet, E. J., and Mudd, S. M., 2009, A theoretical model coupling chemical weathering rates with denudation rates: *Geology*, v. 37, no. 2, p. 151-154.
- Gaillardet, J., Calmels, D., Romero-Mujalli, G., Zakharova, E., and Hartmann, J., 2018, Global climate control on carbonate weathering intensity: *Chemical Geology*.
- Gaillardet, J., Dupré, B., Louvat, P., and Allègre, C. J., 1999, Global silicate weathering and CO₂ consumption rates deduced from the chemistry of large rivers: *Chemical Geology*, v. 159, no. 1, p. 3-30.
- 635 Galy, A., and France-Lanord, C., 1999, Weathering processes in the Ganges–Brahmaputra basin and the riverine alkalinity budget: *Chemical Geology*, v. 159, no. 1–4, p. 31-60.
- Godsey, S. E., Hartmann, J., and Kirchner, J. W., 2019, Catchment chemostasis revisited: Water quality responds differently to variations in weather and climate: *Hydrological Processes*, v. 33, no. 24, p. 3056-3069.
- 640 Guo, J., Ma, L., Gaillardet, J., Sak, P. B., Pereyra, Y., and Engel, J., 2019, Reconciling chemical weathering rates across scales: Application of uranium-series isotope systematics in volcanic weathering clasts from Basse-Terre Island (French Guadeloupe): *Earth and Planetary Science Letters*, p. 115874.
- Hartmann, J., Jansen, N., Dürr, H. H., Kempe, S., and Köhler, P., 2009, Global CO₂-consumption by chemical weathering: What is the contribution of highly active weathering regions?: *Global and Planetary Change*, v. 69, no. 4, p. 185-194.
- 645 Hilley, G. E., Chamberlain, C. P., Moon, S., Porder, S., and Willett, S. D., 2010, Competition between erosion and reaction kinetics in controlling silicate-weathering rates: *Earth and Planetary Science Letters*, v. 293, no. 1–2, p. 191-199.
- Hilton, R. G., and West, A. J., 2020, Mountains, erosion and the carbon cycle: *Nature Reviews Earth & Environment*, v. 1, no. 6, p. 284-299.
- Huang, M. H., Buick, I. S., and Hou, L. W., 2003, Tectonometamorphic Evolution of the Eastern Tibet Plateau: Evidence from the Central Songpan–Garzè Orogenic Belt, Western China: *Journal of Petrology*, v. 44, no. 2, p. 255-278.
- 650 Ibarra, D. E., Caves, J. K., Moon, S., Thomas, D. L., Hartmann, J., Chamberlain, C. P., and Maher, K., 2016, Differential weathering of basaltic and granitic catchments from concentration–discharge relationships: *Geochimica et Cosmochimica Acta*, v. 190, p. 265-293.
- Jacobson, A. D., and Blum, J. D., 2003, Relationship between mechanical erosion and atmospheric CO₂ consumption in the New Zealand Southern Alps: *Geology*, v. 31, no. 10, p. 865-868.
- 655 Jacobson, A. D., Blum, J. D., Chamberlain, C. P., Craw, D., and Koons, P. O., 2003, Climatic and tectonic controls on chemical weathering in the New Zealand Southern Alps: *Geochimica et Cosmochimica Acta*, v. 67, no. 1, p. 29-46.
- Jiang, H., Liu, W., Xu, Z., Zhou, X., Zheng, Z., Zhao, T., Zhou, L., Zhang, X., Xu, Y., and Liu, T., 2018, Chemical weathering of small catchments on the Southeastern Tibetan Plateau I: Water sources, solute sources and weathering rates: *Chemical Geology*, v. 500, p. 159-174.
- 660 Kemeny, P. C., Lopez, G. I., Dalleska, N. F., Torres, M., Burke, A., Bhatt, M. P., West, A. J., Hartmann, J., and Adkins, J. F., 2021, Sulfate sulfur isotopes and major ion chemistry reveal that pyrite oxidation counteracts CO₂ drawdown from silicate weathering in the Langtang–Trisuli–Narayani River system, Nepal Himalaya: *Geochimica et Cosmochimica Acta*, v. 294, p. 43-69.
- Kemeny, P. C., and Torres, M. A., 2021, Presentation and applications of mixing elements and dissolved isotopes in rivers (MEANDIR), a customizable MATLAB model for Monte Carlo inversion of dissolved river chemistry: *American Journal of Science*, v. 321, no. 5, p. 579-642.
- 665 Kump, L. R., and Arthur, M. A., 1997, Global Chemical Erosion during the Cenozoic: Weatherability Balances the Budgets, *in* Ruddiman, W. F., ed., *Tectonic Uplift and Climate Change*: Boston, MA, Springer US, p. 399-426.
- Larsen, I. J., Almond, P. C., Eger, A., Stone, J. O., Montgomery, D. R., and Malcolm, B., 2014, Rapid Soil Production and Weathering in the Southern Alps, New Zealand: *Science*, v. 343, no. 6171, p. 637-640.
- 670 Li, G., Hartmann, J., Derry, L. A., West, A. J., You, C.-F., Long, X., Zhan, T., Li, L., Li, G., Qiu, W., Li, T., Liu, L., Chen, Y., Ji, J., Zhao, L., and Chen, J., 2016, Temperature dependence of basalt weathering: *Earth and Planetary Science Letters*, v. 443, p. 59-69.
- Maffre, P., Swanson-Hysell, N. L., and Goddérís, Y., 2021, Limited Carbon Cycle Response to Increased Sulfide Weathering Due to Oxygen Feedback: *Geophysical Research Letters*, v. 48, no. 19, p. e2021GL094589.
- Märki, L., Lupker, M., France-Lanord, C., Lavé, J., Gallen, S., Gajurel, A. P., Haghipour, N., Leuenberger-West, F., and Eglinton, T., 2021, An unshakable carbon budget for the Himalaya: *Nature Geoscience*.
- 675 Meybeck, M., 1987, Global chemical weathering of surficial rocks estimated from river dissolved loads: *American Journal of Science*, v. 287, no. 5, p. 401-428.
- Moon, S., Chamberlain, C. P., and Hilley, G. E., 2014, New estimates of silicate weathering rates and their uncertainties in global rivers: *Geochimica et Cosmochimica Acta*, v. 134, p. 257-274.

- 680 Morse, J. W., and Arvidson, R. S., 2002, The dissolution kinetics of major sedimentary carbonate minerals: *Earth-Science Reviews*, v. 58, no. 1–2, p. 51-84.
- Niemi, N. A., Oskin, M., Burbank, D. W., Heimsath, A. M., and Gabet, E. J., 2005, Effects of bedrock landslides on cosmogenically determined erosion rates: *Earth and Planetary Science Letters*, v. 237, no. 3–4, p. 480-498.
- 685 Oeser, R. A., and von Blanckenburg, F., 2020, Do degree and rate of silicate weathering depend on plant productivity?: *Biogeosciences*, v. 17, no. 19, p. 4883-4917.
- Ouimet, W. B., Whipple, K. X., and Granger, D. E., 2009, Beyond threshold hillslopes: Channel adjustment to base-level fall in tectonically active mountain ranges: *Geology*, v. 37, no. 7, p. 579-582.
- Raymo, M. E., and Ruddiman, W. F., 1992, Tectonic forcing of late Cenozoic climate: *Nature*, v. 359, no. 6391, p. 117-122.
- 690 Relph, K. E., Stevenson, E. I., Turchyn, A. V., Antler, G., Bickle, M. J., Baronas, J. J., Darby, S. E., Parsons, D. R., and Tipper, E. T., 2021, Partitioning riverine sulfate sources using oxygen and sulfur isotopes: Implications for carbon budgets of large rivers: *Earth and Planetary Science Letters*, v. 567, p. 116957.
- Riebe, C. S., and Granger, D. E., 2013, Quantifying effects of deep and near-surface chemical erosion on cosmogenic nuclides in soils, saprolite, and sediment: *Earth Surface Processes and Landforms*, v. 38, no. 5, p. 523-533.
- Riebe, C. S., Kirchner, J. W., and Finkel, R. C., 2004, Erosional and climatic effects on long-term chemical weathering rates in granitic landscapes spanning diverse climate regimes: *Earth and Planetary Science Letters*, v. 224, no. 3–4, p. 547-562.
- 695 Riebe, C. S., Kirchner, J. W., Granger, D. E., and Finkel, R. C., 2001, Strong tectonic and weak climatic control of long-term chemical weathering rates: *Geology*, v. 29, no. 6, p. 511-514.
- Roger, F., Jolivet, M., and Malavieille, J., 2010, The tectonic evolution of the Songpan-Garzê (North Tibet) and adjacent areas from Proterozoic to Present: A synthesis: *Journal of Asian Earth Sciences*, v. 39, no. 4, p. 254-269.
- 700 Roger, F., Malavieille, J., Leloup, P. H., Calassou, S., and Xu, Z., 2004, Timing of granite emplacement and cooling in the Songpan–Garzê Fold Belt (eastern Tibetan Plateau) with tectonic implications: *Journal of Asian Earth Sciences*, v. 22, no. 5, p. 465-481.
- Searle, M. P., Roberts, N. M. W., Chung, S.-L., Lee, Y.-H., Cook, K. L., Elliott, J. R., Weller, O. M., St-Onge, M. R., Xu, X.-W., Tan, X.-B., and Li, K., 2016, Age and anatomy of the Gongga Shan batholith, eastern Tibetan Plateau, and its relationship to the active Xianshui-he fault: *Geosphere*, v. 12, no. 3, p. 948-970.
- 705 Spence, J., and Telmer, K., 2005, The role of sulfur in chemical weathering and atmospheric CO₂ fluxes: Evidence from major ions, $\delta^{13}\text{CDIC}$, and $\delta^{34}\text{SSO}_4$ in rivers of the Canadian Cordillera: *Geochimica et Cosmochimica Acta*, v. 69, no. 23, p. 5441-5458.
- Tipper, E. T., Bickle, M. J., Galy, A., West, A. J., Pomiès, C., and Chapman, H. J., 2006, The short term climatic sensitivity of carbonate and silicate weathering fluxes: Insight from seasonal variations in river chemistry: *Geochimica et Cosmochimica Acta*, v. 70, no. 11, p. 2737-2754.
- 710 Tipper, E. T., Stevenson, E. I., Alcock, V., Knight, A. C. G., Baronas, J. J., Hilton, R. G., Bickle, M. J., Larkin, C. S., Feng, L., Relph, K. E., and Hughes, G., 2021, Global silicate weathering flux overestimated because of sediment–water cation exchange: *Proceedings of the National Academy of Sciences*, v. 118, no. 1, p. e2016430118.
- Tofelde, S., Duesing, W., Schildgen, T. F., Wickert, A. D., Wittmann, H., Alonso, R. N., and Strecker, M., 2018, Effects of deep-seated versus shallow hillslope processes on cosmogenic ¹⁰Be concentrations in fluvial sand and gravel: *Earth Surface Processes and Landforms*, v. 43, no. 15, p. 3086-3098.
- 715 Torres, M. A., West, A. J., Clark, K. E., Paris, G., Bouchez, J., Ponton, C., Feakins, S. J., Galy, V., and Adkins, J. F., 2016, The acid and alkalinity budgets of weathering in the Andes–Amazon system: Insights into the erosional control of global biogeochemical cycles: *Earth and Planetary Science Letters*, v. 450, p. 381-391.
- Torres, M. A., West, A. J., and Li, G., 2014, Sulphide oxidation and carbonate dissolution as a source of CO₂ over geological timescales: *Nature*, v. 507, no. 7492, p. 346-349.
- 720 Uhlig, D., and von Blanckenburg, F., 2019, How Slow Rock Weathering Balances Nutrient Loss During Fast Forest Floor Turnover in Montane, Temperate Forest Ecosystems: *Frontiers in Earth Science*, v. 7, no. 159.
- Walker, J. C. G., Hays, P. B., and Kasting, J. F., 1981, A negative feedback mechanism for the long-term stabilization of Earth's surface temperature: *Journal of Geophysical Research: Oceans*, v. 86, no. C10, p. 9776-9782.
- 725 Weller, O. M., St-Onge, M. R., Waters, D. J., Rayner, N., Searle, M. P., Chung, S.-L., Palin, R. M., Lee, Y.-H., and Xu, X., 2013, Quantifying Barrovian metamorphism in the Danba Structural Culmination of eastern Tibet: *Journal of Metamorphic Geology*, v. 31, no. 9, p. 909-935.
- West, A. J., 2012, Thickness of the chemical weathering zone and implications for erosional and climatic drivers of weathering and for carbon-cycle feedbacks: *Geology*, v. 40, no. 9, p. 811-814.
- 730 West, A. J., Galy, A., and Bickle, M., 2005, Tectonic and climatic controls on silicate weathering: *Earth and Planetary Science Letters*, v. 235, no. 1–2, p. 211-228.
- White, A. F., and Blum, A. E., 1995, Effects of climate on chemical weathering in watersheds: *Geochimica et Cosmochimica Acta*, v. 59, no. 9, p. 1729-1747.
- 735 White, A. F., Bullen, T. D., Vivit, D. V., Schulz, M. S., and Clow, D. W., 1999, The role of disseminated calcite in the chemical weathering of granitoid rocks: *Geochimica et Cosmochimica Acta*, v. 63, no. 13, p. 1939-1953.

Williamson, M. A., and Rimstidt, J. D., 1994, The kinetics and electrochemical rate-determining step of aqueous pyrite oxidation: *Geochimica et Cosmochimica Acta*, v. 58, no. 24, p. 5443-5454.

Yanites, B. J., Tucker, G. E., and Anderson, R. S., 2009, Numerical and analytical models of cosmogenic radionuclide dynamics in landslide-dominated drainage basins: *Journal of Geophysical Research: Earth Surface*, v. 114, no. F1.

740 Zeebe, R. E., and Westbrook, P., 2003, A simple model for the CaCO₃ saturation state of the ocean: The “Strangelove,” the “Neritan,” and the “Cretan” Ocean: *Geochemistry, Geophysics, Geosystems*, v. 4, no. 12, p. 1104.